ACS Catalysis

Research Article

pubs.acs.org/acscatalysis

Ultrathin Platinum Films for Methanol and Formic Acid Oxidation: Activity as a Function of Film Thickness and Coverage

Sang Hyun Ahn, Yihua Liu, and Thomas P. Moffat*

Materials Science and Engineering Division, Material Measurement Laboratory, National Institute of Standard and Technology (NIST), 100 Bureau Drive, Gaithersburg, Maryland 20899, United States

Supporting Information

ABSTRACT: Self-terminating electrodeposition was used to grow ultrathin Pt overlayers on 111 textured Au thin films. The Pt thickness was digitally controlled by pulsed potential deposition that enabled the influence of overlayer thickness on electrocataytic reactions, such as methanol and formic acid oxidation, to be examined. Bimetallic and ensemble effects associated with submonolayer coverage of Pt on Au yield enhanced catalysis. For films grown using one deposition pulse, the peak rate of CH_3OH oxidation was enhanced by a factor of 4 relative to bulk Pt. The overlayer consisted of 2 nm diameter monolayer Pt islands that covered 75% of the surface; however, voltammetric cycling resulted in a loss of the enhanced activity associated with the as-deposited submonolayer films. For thicker Pt films, the electrocatalytic activity decreased monotonically with thickness until bulk Pt behavior was obtained beyond three monolayers. For HCOOH oxidation improvements in the Pt area, normalized activity in excess of a 100-fold were observed for submonolayer Pt films. The performance improved with voltammetric cycling as a result of a combination of Pt dissolution, Au segregation, and Pt−Au alloy formation. The maximum activity was associated with fractional surface coverage between 0.28 and 0.21, although the films were subject to a deactivation process at longer times related to a diffusional process. Bulk Pt behavior for formic acid oxidation was observed for Pt films greater than three monolayers in thickness.

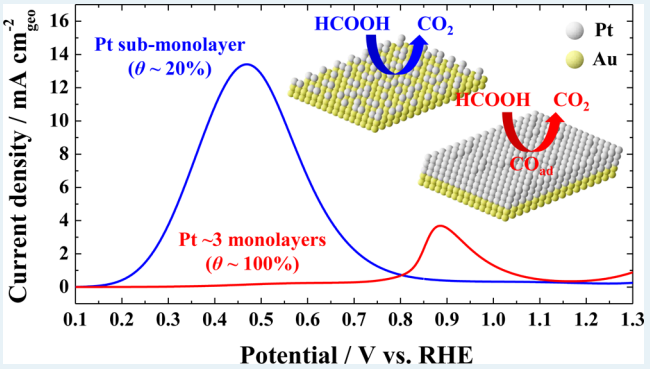

KEYWORDS: *ultrathin platinum film, self-terminating electrodeposition, methanol oxidation, formic acid oxidation, platinum−gold bimetallic ensemble effect*

1. INTRODUCTION

Fuel cells have long been recognized as a promising technology that offers the potential of high energy conversion efficiency with environmentally friendly emission characteristics. Much effort has focused on H_2 as the ultimate clean fuel; however, the convenience of liquid fuels for transportation application and simplicity of storage has encouraged examination of small organic molecules as alternative energy carriers.[1,2] The absence of C−C bonds along with the high hydrogen-to-carbon ratio in methanol and formic acid offers the prospect of reasonable oxidation kinetics and the complete conversion to CO_2 at low operating temperature. These characteristics have motivated the development of direct methanol fuel cell[3] and direct formic acid fuel cell[4] as portable energy conversion devices. Nevertheless, large-scale commercialization remains constrained by the limited performance and high cost of existing Pt-group metal electrocatalysts. Surface orientation of Pt may be used to tune the oxidation kinetics of methanol and formic acid;[5−9] however, to further improve the situation, two strategies are being explored, namely, enhanced catalytic performance by alloying and minimization of Pt-group metal loading, by using architectures that maximize the area/volume ratio of the expensive metals. These strategies merge when minimization of materials usage is facilitated by the formation of ultrathin Pt-group metal overlayers on different substrates where the combination of ligand, strain, ensemble, or alloying interactions on the bimetallic surface may offer enhanced activity toward multistep fuel oxidation or the oxygen reduction reaction relevant to fuel cells. For example, a notable increase in the intrinsic activity for electrochemical oxidation of methanol and formic acid has been reported for ultrathin Pt films deposited on Au, despite the inactive nature of the Au substrate itself.[10−27]

The positive influence of a Pt overlayer has largely been attributed to either strain[10−12] or ensemble effects.[14,19−21] Discerning between these effects is dependent upon knowledge of, or assumptions about, the structure and composition of the bimetallic electrodes. Spectroscopic studies of reaction intermediates[1,2,10,18,20] offer mechanistic insight, and density functional theory (DFT) has been used to evaluate the effect of substrate-induced tensile strain on the electronic character of Pt overlayers on various substrates.[10,18,28] Nevertheless, rigorous

Received: August 20, 2014
Revised: February 18, 2015
Published: February 19, 2015

DOI: 10.1021/cs501228j
ACS Catal. 2015, 5, 2124−2136

comparison between idealized models of interface structure versus the heterogeneous and defective nature of most practical catalyst surfaces remains a challenging and underdeveloped subject.

Current fuel cell electrodes mostly take the form of either Pt nanoparticle carbon composites[29] or nanostructured thin films.[30] Thin Pt skins are developed on various metal, alloy, or nonmetal substrates, by some combination of segregation, dealloying, or deposition processes. An important subset of these methods are inexpensive chemical processes for growing ultrathin and submonolayer Pt films on various materials to enable the exploration of catalytic properties as a function of overlayer thickness and substrate identity.[10−20] Multistep galvanic exchange reactions, in which a wetting layer of underpotential deposited metal is used to reduce Pt, have been widely employed; however, some portion of the reducing agent (e.g. Cu, Pb) is often incorporated as an alloying agents within the growing Pt overlayer.[10,20,31−34] Herein, we use a recently developed self-terminating electrodeposition process that enables rapid formation of ultrathin Pt films.[35] The pulsed potential controlled process may be viewed as a wet form of atomic layer deposition whereby underpotential-deposited H (H_{upd}) competes with $PtCl_4^{2-}$ adsorption for the available surface sites and leads to quenching of the deposition process under certain conditions. The surface may be reactivated for additional deposition by pulsing the potential to selectively oxidize the H_{upd}, thereby enabling additional $PtCl_4^{2-}$ to be adsorbed, followed by its reduction during a subsequent negative-going potential pulse.[35,36] After the first deposition pulse, most of the Au surface is covered by two-dimensional Pt islands with subsequent cycles, leading to coalescence and incremental deposition of thicker layers. In this work, self-terminated deposition is used to grow ultrathin Pt films of variable thickness on Au to investigate the catalytic behavior of such materials for methanol and formic acid oxidation and its dependence on overlayer thickness. Cyclic voltammetry (CV) and X-ray photoelectron spectroscopy (XPS) were used to quantify the performance and degradation of the ultrathin Pt catalyst film during potential cycling.

2. EXPERIMENTAL SECTION

2.1. Electrodeposition of Pt. Ultrathin Pt films were deposited on 111 textured Au thin films using the recently developed self-terminating electrodeposition procedure.[35] The Au substrates were prepared by e-beam evaporation of 150 nm of Au on a 5 nm Ti adhesion layer supported on a Si (100) wafer. Prior to Pt electrodeposition, organic residues were removed from the Au substrates by immersion in Caro's (piranha) solution, 75% H_2SO_4 + 25% H_2O_2, for 10 min, followed by rinsing with 18 MΩ water. Electrodeposition was performed using an electrolyte composed of 3 mmol/L K_2PtCl_4 and 0.5 mol/L NaCl at pH = 3.5 in a conventional three electrode cell with a Pt counter electrode and a sodium chloride-saturated, calomel reference electrode (SSCE). Self-terminating deposition of a Pt monolayer film was performed by stepping the potential to −0.8 V_{SSCE} for 5 s, followed by stepping back to +0.4 V_{SSCE}, whereupon the specimen was removed from the cell and quickly rinsed in H_2-saturated 18 MΩ water. For growing thicker Pt overlayers, the process was repeated by stepping between −0.8 V_{SSCE} for 5 s and +0.4 V_{SSCE} for 30 s for the desired number of cycles. The films were examined by XPS using a Kratos AXIS Ultra DLD spectrometer with an Al K_α monochromatic source operating at a base pressure of 3×10^{-10} Torr. The energy scale of the spectrometer was calibrated with respect to the Au $4f_{7/2}$ peak at 83.98 eV.[37] The Casa XPS program was used to analyze the spectra using a Shirley background in the fitting of high resolution 4f spectra. The thickness of the as-deposited Pt overlayer, d, was quantified from the measured Pt 4f/Au 4f integrated peak area ratio using a simple homogeneous overlayer model for the attenuation of the respective photoelectrons as given by the following equation:[38]

$$d = \lambda_{AL} \cos\theta \ln[1 + (I_{Pt}/s_{Pt})/(I_{Au}/s_{Au})] \quad (1)$$

where λ_{AL} is the attenuation length of 1415 eV photoelectrons in the Pt overlayer (λ_{AL} = 1.252 nm) determined by interpolation from data in Table 1 of ref 38, I is the peak intensity for Pt 4f and Au 4f photoelectrons, s is the elemental sensitivity factors (s_{Pt} = 5.575, s_{Au} = 6.250), and θ is the takeoff angle between the surface normal and the entrance of the electron analyzer 0° in the present experiments.

2.2. Electroactive Area. The electroactive area of the Pt films was assayed voltammetrically in both 0.1 mol/L $HClO_4$ and 0.5 mol/L H_2SO_4 by measuring the underpotential deposited hydrogen, H_{upd}, charge using a scan rate of 20 mV/s. In a subset of experiments, the oxide formation and reduction waves were also examined. Freshly deposited specimens were used for each experiment, and the specimens were transferred to the electrolyte of interest using a H_2-saturated water droplet to protect the Pt surface. A Pt wire counter electrode and trapped H_2 reference electrode (RHE, V_{RHE}) were used in these experiments and held in separate fritted compartments while the electrolyte in the working electrode compartment was deoxygenated with Ar before and during the experiments.

2.3. Fuel Oxidation Measurements. Methanol oxidation was measured in 0.1 mol/L $HClO_4$ + 0.5 mol/L CH_3OH, and formic acid oxidation was evaluated in 0.5 mol/L H_2SO_4 + 0.5 mol/L HCOOH. The methanol (128224 Fischer Scientific) and formic acid (33015 Sigma-Aldich) were both ACS reagent grade. The methanol contained <0.001% carbonyl compounds, and the formic acid contained <0.005% acetic acid. A saturated potassium sulfate/mercurous sulfate/mercury reference electrode (SSE) was used for the electroanalytical measurements. The data are presented on the RHE scale on the basis of a conversion factor derived from emf measurements between the Pt counter electrode and the SSE reference electrode in hydrogen-saturated 0.1 mol/L $HClO_4$ and 0.5 mol/L H_2SO_4 to give conversion factors of 0 V_{SSE} = 0.72 V_{RHE} and 0 V_{SSE} = 0.70 V_{RHE}, respectively. The reference and counter electrodes were held in separate compartments isolated from the main cell by fritted junctions. Freshly deposited specimens were transferred to the fuel-containing electrolytes using a H_2-saturated water droplet to protect the Pt surface. The electrolytes were purged by Ar gas to remove the dissolved oxygen prior to fuel oxidation measurments, and the gas flow was maintained over the electrolyte during the measurements. For reference purposes, the catalytic activity of a mechanically polished Pt rotating disk electrode (RDE) was also measured.

3. RESULTS AND DISCUSSION

3.1. Electrode Preparation and Characterization. The electrocatalytic perfomance of the Pt films was examined as a function of the number of deposition pulses. A representative current transient for a film grown using 7 deposition pulses to −0.8 V_{SSCE} is shown in Figure 1a. Pt 4f and Au 4f XPS spectra

DOI: 10.1021/cs501228j
ACS Catal. 2015, 5, 2124−2136

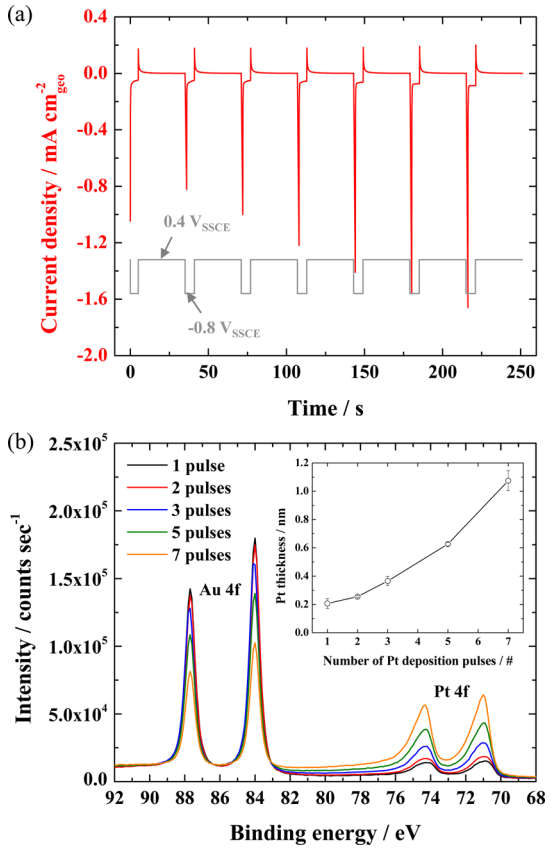

Figure 1. (a) Current transient for a Pt ultrathin film deposited using seven deposition pulses. (b) Pt 4f and Au 4f XPS spectra for Pt ultrathin films deposited using 1, 2, 3, 5, and 7 deposition pulses (inset: Pt thickness calculated by Pt 4f/Au 4f peak ratio). Error bars represent the standard deviation of spectra collected at 4–6 different locations per specimen.

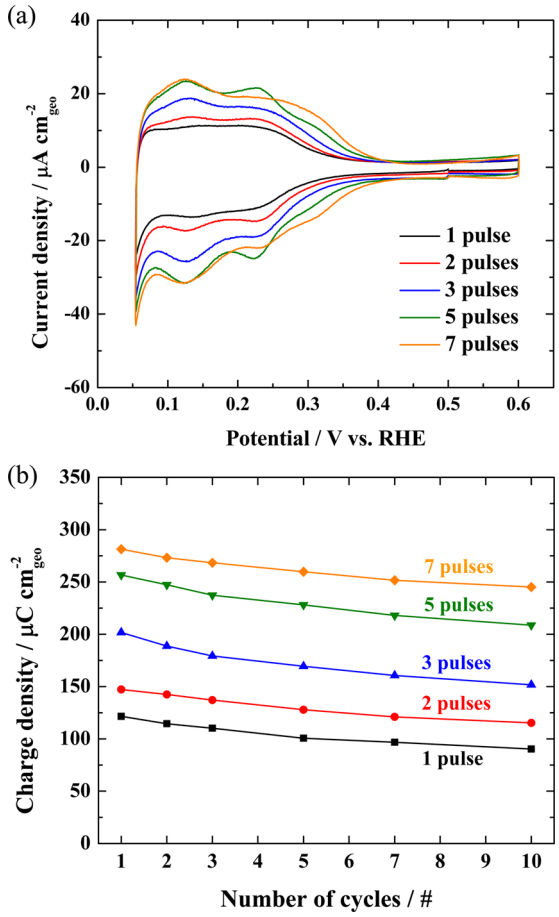

Figure 2. (a) First voltammetric cycle for H_{upd} as a function of the number of Pt deposition pulses, recorded in Ar-purged 0.1 mol/L $HClO_4$ with a scan rate of 20 mV/s. (b) Calculated H_{upd} charge density for the respective ultrathin Pt films during the first 10 voltammetric cycles.

for films grown for 1, 2, 3, 5, and 7 pulses are given in Figure 1b, with the calculated thickness of the respective Pt overlayers shown in the inset. For one deposition pulse, the Pt overlayer is close to a monolayer, in good agreement with prior work in which a scanning tunneling microscope (STM) indicated a fractional surface coverage close to 0.85.[35] For the second deposition pulse, the Pt overlayer thickness increases, although the increment is substantially less than that associated with the first pulse. For subsequent deposition pulses, the incremental thickness progressively increases to exceed that associated with the first layer. This is also evident in the increase in peak current of the transients shown in Figure 1a. The variations in thickess of the multicycle films from that in previous work[35,36] reflect the convolution of the electrochemical cell time constant, a variable between the different experiments, and the growth process, as will be detailed in another publication.

H_{upd} was used to probe the coverage and surface structure of the Pt overlayer. The as-deposited films, covered with a H_2-saturated water droplet, were transferred to the cell containing 0.1 mol/L $HClO_4$. The first voltammetric cycle for each film is shown in Figure 2a. The flat, square shaped H_{upd} waves for the one deposition pulse film is similar to that reported for H_{upd} on Pt (111).[39] The H_{upd} charge was determined by integrating the current between and +0.05 and +0.50 V_{RHE} and taking the average of the adsorption and desorption charge and subtracting the double layer capacitance measured by extrapolation from the double layer voltammetric region. The measured charge of ~120 $\mu C/cm^2$ compares with 160 $\mu C/cm^2$ reported for Pt (111).[39] The value of 160 $\mu C/cm^2$ is congruent with H_{upd} being associated primarily with H occupancy of fcc 3-fold hollow sites on the Pt (111) islands.[40,41] An STM study[35] of self-terminated Pt deposition on Au (111) indicate a fractional Pt island coverage of 0.85; the H_{upd} charge for Pt islands on the 111 texture of the Au substrate in the present work indicates a fractional Pt island coverage of ~0.75.

For multipulse Pt deposition, the shape of the H_{upd} feature progressively deviates from the flat broad wave to develop peaks that have been ascribed to H_{upd} occurring on other low-index Pt surfaces or highly stepped surfaces.[42] The increase in charge largely reflects the growth in roughness associated with the thicker Pt overlayers and the development of some 110, 100, and higher index surface segments. During the first deposition pulse, Pt deposition involves the reduction of adsorbed $PtCl_4^{2-}$ on Au to form islands complemented by the reduction of solvated species at the island perimeter, while H_{upd} on top of the Pt islands prevents further deposition from occurring on top of the freshly formed island terraces. In contrast, for subsequent deposition pulses, once the adsorbed $PtCl_4^{2-}$ species have been reduced (amounting to ~0.13 fractional coverage), H_{upd} directly competes with solvated $PtCl_4^{2-}$ for the available surface sites. The $PtCl_4^{2-}$ species that do find unblocked sites initiate the onset of 3-D growth

DOI: 10.1021/cs501228j
ACS Catal. 2015, 5, 2124–2136

supported by the high intrinsic step-edge barrier for Pt on Pt growth and the absence of neighboring Au regions that would otherwise facilitate lateral expansion of Pt islands. The incipient roughness leads to incremental increases in the H_{upd} pseudocapacitance with each deposition pulse and a corresponding increase in the electrochemical cell time constant. The resulting lag in electrode charging during potential pulsing between +0.4 V_{SSCE} and −0.8 V_{SSCE} results in ever increasing increments of conventional overpotential deposition during multipulse deposition.

The stability of the electrodes was monitored during multicycle voltammetry. A selection from the first 10 voltammetric cycles reveals the change in shape and decreased magnitude of the H_{upd} waves as shown in Figure S1. The H_{upd} charge is summarized in Figure 2b. Inspection of Figure S1 reveals that the evolution of H_{upd} waves for the Pt film grown for seven deposition pulses is quite similar to that of the mechanically polished bulk Pt RDE. In contrast, for the thinner Pt overlayers, proportionately greater changes in shape occur. The low surface energy associated with Au favors its segregation to the free surface, at least in the double layer region, and may account for some of the lost H_{upd} activity congruent with other reports.[43,44]

3.2. Methanol Oxidation. The kinetics of methanol oxidation on ultrathin Pt films were examined as a function of the thickness as specified by the number of self-terminating deposition pulses. Following electrodeposition, the films were transferred under H_2-saturated water droplet and immersed into 0.5 mol/L CH_3OH and 0.1 mol/L $HClO_4$ at +0.3 V_{RHE}. The first voltammetric cycle for each film, normalized by the projected geometrical electrode area, is shown in Figure 3a. The onset of fuel oxidation occurs near +0.60 V_{RHE} for all the electrodes examined. The current increases with potential passing through a maximum due to oxide formation that inhibits further methanol oxidation. The inhibition is lifted with the reduction of the oxide on the negative going sweep. The Pt monolayer film grown using one deposition pulse exhibits the highest peak activity for methanol oxidation based on the geometric projected surface area. Negligible activity was evident for the Au thin substrate itself. Normalizing the current density to the H_{upd} charge measured for the respective freshly deposited Pt films (i.e., Figure 2) gives the methanol oxidation rate in terms mA/μC_{Hupd} for the first positive going sweep, as shown in Figure 3b. The Pt submonolayer film, grown with one depositon pulse, exhibits a H_{upd} normalized peak current that is almost 4 times greater than that of bulk Pt. In contrast, the Pt films grown for three or more deposition pulses, which correspond to thicknesses beyond two monolayers, yield methanol oxidation kinetics that are almost identical to that of bulk Pt. For Pt films grown using two deposition pulses, the rate of fuel oxidation lies between these two limits.

The enhanced catalytic response of the submonolayer Pt films, compared with the thicker Pt films that exhibit the behavior of bulk Pt, indicates an important contribution by the Au substrate. Favorable catalytic activity of Pt layers on Au has also been noted for films[10,12,14−16] and nanoparticles[10,11,13,17] produced by other means. The improved performance was attributed to a variety of mechanisms from an electronic or ligand effect, to strain driven shifts of the d-band position, or ensemble effects. The thickness dependence revealed in the present study suggests the observed enhancement is due to contributions that arise from the proximity of exposed Au substrate sites and the Pt overlayer or, more specifically, the

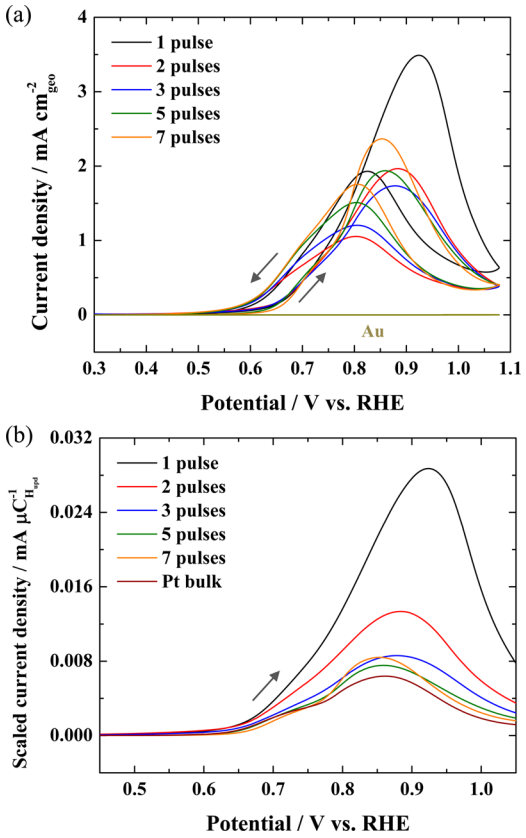

Figure 3. First voltammetric cycle for methanol oxidation on Pt ultrathin films, bulk Pt, and Au in Ar-purged 0.5 mol/L CH_3OH + 0.1 mol/L $HClO_4$ solution for a scan rate of 10 mV/s. (a) Cyclic voltammetry scaled by geometrical area and (b) cyclic voltammetry scaled by H_{upd} charge (forward scan only).

step sites that surround the Pt islands. It is noteworthy that the enhanced methanol oxidation response occurs in the potential regime coincident with the onset of Pt oxidation in perchloric acid, as evident in Figure 4a. For thicker Pt films, the Au substrate is effectively covered, and the electrode activity reverts to the characteristics of bulk Pt. This occurs even though the effects of substrate strain and its electronic perturbation on the overlayer are still to be expected for thin fully coalesced films. Consequently, the strain associated with misfit may not be the predominant driver for the enhanced catalytic response, in contrast to recent arguments advanced on the basis of DFT calculations.[10] The computational work assumed a continuous fully coalesced overlayer was formed after one cycle of the surface-limited redox replacement reaction (SLRR). However, literature images of films grown by SLRRs indicate that one exchange cycle fails to yield fully coalesced overlayers; rather, multiple cycles were required before complete coverage was attained.[45,46] Furthermore, these SLRR films often incorporate measurable amounts of the reducing agent (e.g., Cu_{upd} and Pb_{upd}) that are both known to exert additional catalytic effects on the oxidation of organic fuels and complicate analysis of the reactivity of Pt/Au system.[47,48]

For the self-terminated Pt electrodeposition reaction used in the present work, STM studies reveal that the film deposited on Au (111) using one potential pulse has Pt islands with an average diameter near 2 nm and a fractional surface coverage of 0.85.[35] For growth on low-index single crystal (or highly texture thin film) surfaces, this amounts to a huge (significant) increase

DOI: 10.1021/cs501228j
ACS Catal. 2015, 5, 2124−2136

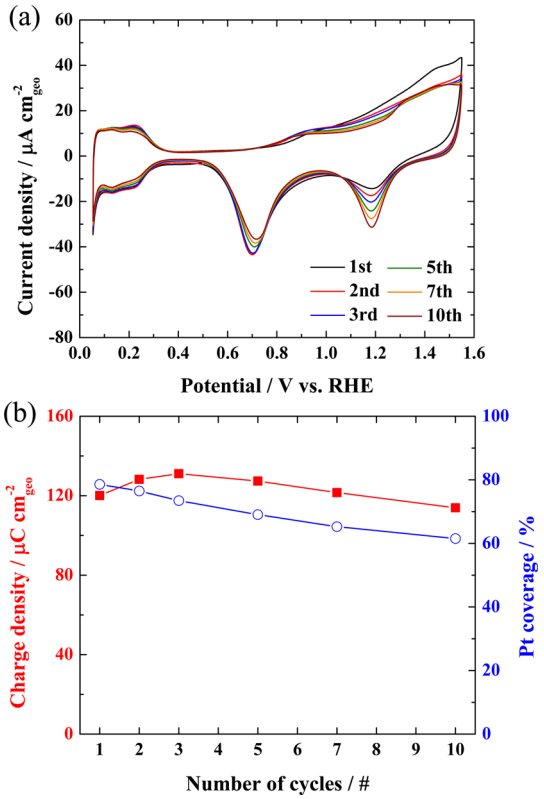

Figure 4. (a) Voltammetric evolution of an ultrathin Pt film, grown using one pulse deposition, in Ar-purged 0.1 mol/L $HClO_4$ using a scan rate of 20 mV/s for10 cycles. (b) Calculated charge densities and fractional Pt coverage from H_{upd} and the ratio of Pt and Au oxide reduction waves.

in the step density. Studies of methanol oxidation of well-defined vicinal Pt surfaces have shown a strong dependence of the rate of reaction on step density and geometry,[49] (110)-oriented steps on miscut Pt (111) surfaces being particularly active with more than doubling of the peak methanol oxidation current evident between Pt (221) and Pt (111).

The importance of step sites in methanol oxidation on nanoparticles has also been noted.[50] The steps associated with the high coverage of 2 nm diameter Pt islands on the as-formed films used in the present study are close to isotropic, preventing a simple comparison with prior single crystal results. Nevertheless the role of the high step density and its mixed Pt−Au character may account for the improved catalytic performance observed for these monolayer films. The enhanced response occurs at potentials coincident with the onset of Pt oxidation, as evident by comparing the first positive going voltmmetric sweep in CH_3OH-$HClO_4$ (Figure 3) with that in $HClO_4$ (Figure 4a). The slight suppression of the onset of Pt oxidation during the first voltammetric cycle (Figure 4a) is ascribed to the inhibition of Pt oxidation at step sites due to partial segregation of Au thereon.[44]

Recent theoretical work also indicates that Pt island morphology has significant implications for strain development in monolayer films. For example, compressive strain due to the line tension of steps and finite size or capillarity effects can significantly diminish the tensile strain associated with misfit between Pt and Au.[51] The complexity associated with finite size effects is further strengthened by a recent first principle computational study of the strain and electronic properties of Pt island on different support structures.[52] For islands with a diameter of <3 nm, the substrate exerts minimal influence on the nearest-neighbor Pt−Pt spacing and the proximity of the d band to the Fermi level. Other recent theoretical work also indicates that electronic hybridization effects may dominate strain effects, even for complete monolayer films.[53] The combined observations indicate that strain effects are unlikely to account for the enhanced methanol oxidation activity observed for the submonolayer films grown using one deposition cycle. To date, no theoretical studies have examined the effect of Pt and Au intermixing at step edges on electrocatalytic methanol oxidation, although the important role of such compositional and structural arrangements on Pt−Au surfaces was evident in recent studies of the methanol oxidation of $Pt_{50}Au_{50}$ alloy nanoparticles in which particles with a surface composition between 70 and 90% Pt were up to twice as active as Pt-covered particles.[54] It is clear from the above that further progress will require better measurements and descriptions of the mesoscopic structure and composition of these heterogeneous bimetallic surfaces to reconcile theory and experiment.

The evolution of CH_3OH oxidation with voltammetric cycling was examined for a variety of conditions. A selection from the first 10 cycles for each Pt film is shown in Figure S2. For the Pt film grown using one deposition pulse, the methanol oxidation kinetics degraded monotonically after the third voltammetric cycle. In contrast, for the film grown using two deposition pulses, the methanol oxidation activity first increased with scanning to pass through a maximum between the fifth and seventh voltammetric cycles; however, the maximum did not approach that of the freshly deposited Pt film grown using one deposition pulse. For the thicker Pt films, grown using five or seven deposition pulses, the attenuation of catalytic activity with voltammetric cycling was noticeably less severe.

Deactivation of the Pt submonolayer island structure is clearly more severe than that observed for the thicker Pt overlayers. This is attributed to the ease of surface rearrangements between the Pt islands and exposed Au substrate at the electrode/electrolyte boundary. The restructuring can be driven by both surface energy and strain relief as well as interaction with reaction intermediates.[43,44,55−59] Similar effects of such surface arrangements on reactivity were also evident in studies of equiatomic $Pt_{50}Au_{50}$ nanoparticles, in which a wide range of behaviors were noted as a function of detailed processing conditions.[54]

Extending the upper potential limit during voltammetric cycling introduces additional mechanisms for surface rearrangement that range from significant Pt dissolution to its accumulation via transfer from the counter electrode,[60−62] to intermixing and roughening that accompanies repetitive place exchange reactions associated with oxide formation and reduction, not to mention the associated expansion and coarsening of the step density. In terms of Pt dissolution, inductively coupled plasma-mass spectrometry (ICP−MS) studies have shown that dissolution from a bulk Pt electrode occurs when voltammetric excursions exceed 1.15 V_{RHE}.[61] For voltammetric cycling up to 1.55 V_{RHE}, a Pt mass loss of ∼6 ng/cm^2 cycle is reported for 0.1 mol/L $HClO_4$.[62]

As shown in Figure 4a, cycling a Pt film, grown using one deposition pulse, under these conditions leads to a decrease in the H_{upd} wave and an expansion of the available Au surface sites evident as the increase in the Au oxide reduction wave. The as-deposited submonolayer Pt film, ∼ 0.75 fractional coverage as

DOI: 10.1021/cs501228j
ACS Catal. 2015, 5, 2124−2136

determined from the ratio of the oxide reduction waves, amounts to 364 ng/cm^2, and thus, 10 voltammetric cycles to 1.55 V_{RHE} would correspond to loss of up to ~60 ng/cm^2 or ~16% of the Pt mass based projection from the ICP−MS study. The estimate is congruent with the increase in exposed Au surface area as revealed by the ratio of the respective oxide reduction waves shown in Figure 4a and summarized in Figure 4b. Initially, the H_{upd} charge increased for the first three voltammetric cycles, presumably associated with additional Pt step sites (i.e., 3-D Pt islands) created by the place-exchange reaction during the oxidation−reduction cycle. This was followed by a decay in H_{upd} charge consistent with Pt dissolution and the increase in exposed Au.

The evolution of the methanol oxidation under somewhat less harsh conditions, upper potential limit of 1.08 V_{RHE} (negligible Pt dissolution[62]) shown in Figure S2 or 1.32 V_{RHE} (2.5−3.0 ng/cm^2/cycle Pt dissolution[62]) as shown in Figure 5a,

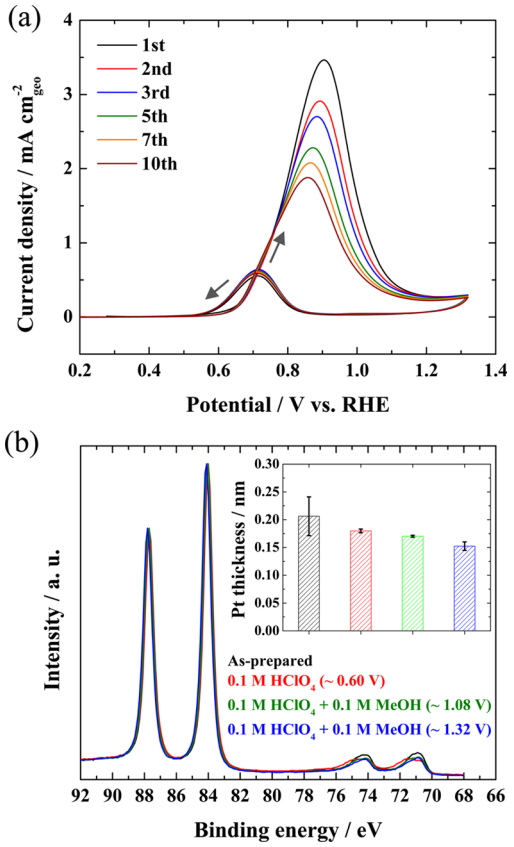

Figure 5. (a) Voltammetric evolution of methanol oxidation on a Pt film grown using one deposition pulse. Voltammetry was performed in Ar-purged 0.5 mol/L CH_3OH + 0.1 mol/L $HClO_4$ solution with a scan rate of 10 mV/s for 10 cycles. (b) Pt 4f and Au 4f XPS spectra for the one-deposition-pulse Pt film before and after 10 voltammetric cycles using the specified upper potential limit. Error bars represent the standard deviation of spectra collected at 4−6 different locations per specimen.

revealed a monotonic decrease in the peak current with cycling that was disproportionately large relative to the loss of Pt coverage revealed by XPS analysis summarized in Figure 5b. Interestingly, the onset of methanol oxidation was not significantly affected for these aging conditions, although the oxidation rate at more positive potentials was negatively impacted. This aging sensitivity of methanol oxidation kinetics in different potential regimes is most likely linked to the adsorption dynamics of reaction intermediates, that is, CO−, −OH, and CH_3OH, and Au segregation to the evolving steps of the initial Pt-rich islands, all of which occur in competition with oxide formation and reduction. The structure and composition of these compositionally mixed regions are strongly history-dependent, with the highest activity associated with the steps of the as-deposited Pt-rich islands and the surrounding open channels of the Au-rich substrate. The major decrease in peak activity evident in Figure 5a is thus attributed to disruption and rearrangements of the structure and composition of the Pt islands, whereas the loss of Pt due to dissolution exerts a less important influence, as suggested by the modest coverage changes shown in Figure 5b.

3.3. Formic Acid Oxidation. The catalytic activity of the ultrathin Pt films toward formic acid oxidation was examined in a solution of 0.5 mol/L HCOOH and 0.5 mol/L H_2SO_4. The Pt films grown using one deposition pulse were substantially more active than bulk Pt, as evident by the 10-fold increase in peak current in the first voltammetric scan for the as-deposited film shown in Figure 6a. For the Pt films grown using five to seven deposition pulses, corresponding to an average Pt thickness in excess of three monolayers, the catalytic behavior reverts to that of bulk Pt. The Au substrate by itself is essentially inactive under these conditions. Scaling the fuel oxidation current by the electroactive H_{upd} area (taken from Figure 2b) indicates a more than 20-fold enhancement in the peak rate of formic acid oxidation on the as-deposited submonolayer Pt film at +0.5 V_{RHE}, as shown in Figure 6b. A Tafel plot of the same data, Figure 6c, reveals the specific activity at 0.4 V_{RHE} for the as-deposited films span almost 2 orders of magnitude between the submonolayer films and bulk Pt. Voltammetric cycling to 0.75 V_{RHE}, which is below the threshold for substantial Pt dissolution (<1.15 V_{RHE}),[61,62] reveals a measurable decrease in activity immediately following the first sweep, although the system exhibits greater stability during subsequent scans (see Figure S3a−e).

Increasing the upper potential limit to 1.30 V_{RHE} leads to significant changes in behavior related to Pt dissolution (see Figure S3g−k) whereby the thinner Pt films exhibit a marked improvement in catalytic activity with cycling. This is evident for Pt films grown using one to three deposition pulses, with the thinnest film showing the most rapid and largest increase in the rate of formic acid oxidation. In contrast, the activity of the thicker films, grown using five or seven deposition pulses, did not significantly change with cycling for the conditions examined.

The positive-going scans for the various films on the 20th voltammetric cycle are shown in Figure 7a. For the thinnest Pt films, the peak formic acid oxidation current increased in magnitude and shifted to more negative potentials, and the secondary peak at +0.9 V_{RHE} decreased. For the Pt films grown using five or seven deposition pulses, the narrow peak at +0.9 V_{RHE} was dominant and reflects acceleration of formic acid oxidation triggered by oxidative removal of poisoning reaction intermediate, that is, CO, from the surface. Interestingly, H_{upd} normalization shown in Figure 7b reveals a similar specific current density for all the films at 0.9 V_{RHE}, indicating that CO-blocked sites persist, even for the thinnest films. At more positive potentials, the electrocatalytic activity is quenched as a result of formation of Pt oxide. The Tafel plot in Figure 7c shows that the specific activity at 0.4 V_{RHE} was enhanced by at least 2 orders of magnitude between the submonolayer film and

DOI: 10.1021/cs501228j
ACS Catal. 2015, 5, 2124−2136

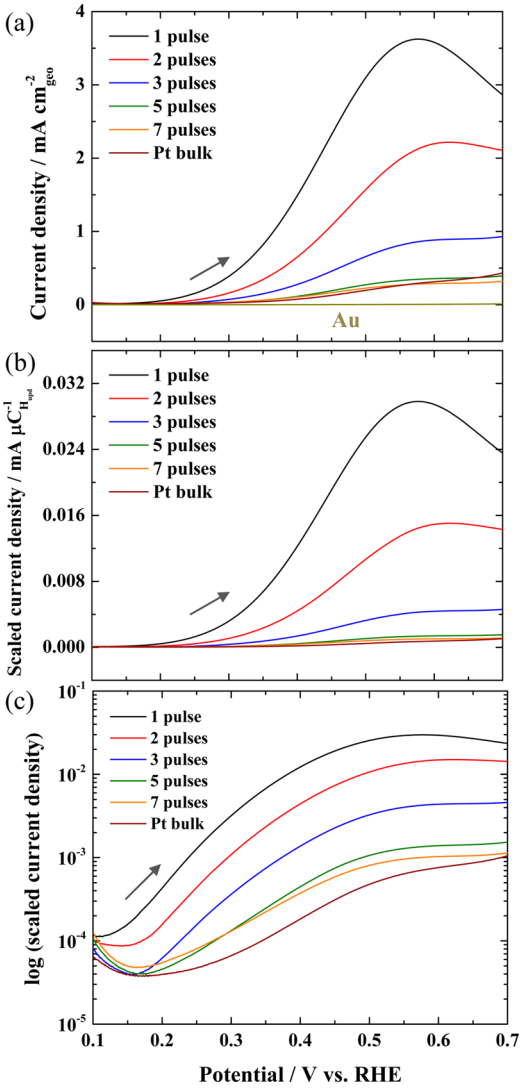

Figure 6. Formic acid oxidation on Pt ultrathin films, bulk Pt, and Au in Ar-purged 0.5 mol/L HCOOH and 0.5 mol/L H_2SO_4 solution for a scan rate of 10 mV/s (forward scan shown for first cycle). (a) Cyclic voltammetry scaled by geometrical area, (b) cyclic voltammetry scaled by H_{upd} charge, and (c) Tafel plots of part b.

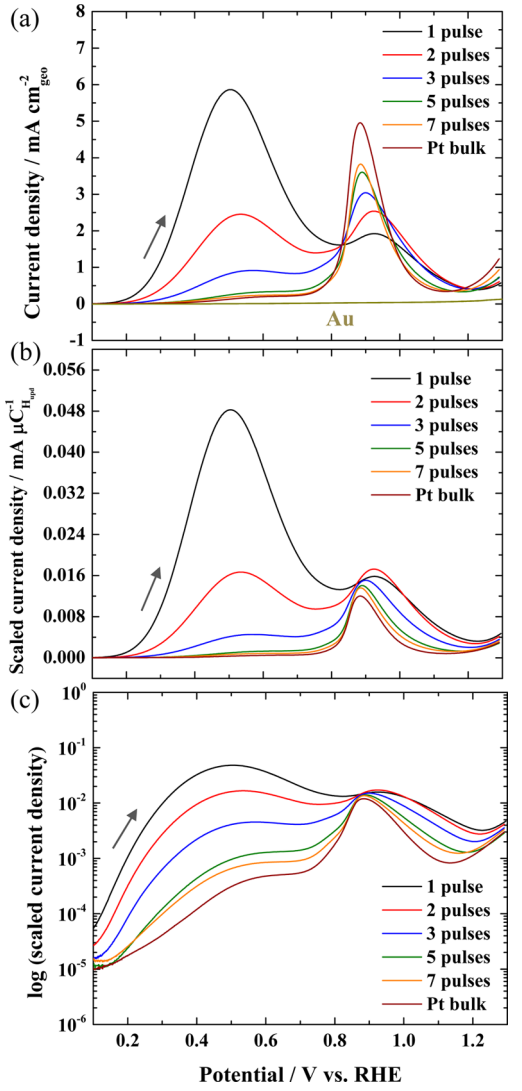

Figure 7. Formic acid oxidation on Pt ultrathin films, bulk Pt, and Au in Ar-purged 0.5 mol/L HCOOH and 0.5 mol/L H_2SO_4 solution for a scan rate of 10 mV/s (20th cycle forward scan shown). (a) Cyclic voltammetry scaled by geometrical area, (b) cyclic voltammetry scaled by H_{upd} charge, and (c) Tafel plots of part b.

bulk Pt. The wide voltammetric window used in Figure 7 reveals two distinct regions of formic acid oxidation behavior related to the direct dehydrogenation mechanism operating at low potentials, whereas the indirect dehydration reaction dominates at higher potentials. The relative contribution of each reaction path reflects the density of neighboring Pt−Au sites. Enhanced HCOOH oxidation activity for a submonolayer coverage of Pt on Au has been previously reported for both planar electrodes[14,19,26] and nanoparticles.[18,20−24] In both cases, the increased reactivity was attributed to ensemble effects that bias formic acid oxidation via the dehydrogenation path. The boundary between the Pt-rich islands and the Au substrate may be central to the activity at low overpotentials, whereas at more positive potentials, the indirect path via CO formation and stripping remains operational on the Pt-rich islands and step sites that still remain for the aging conditions examined thus far.

The important role of the upper potential limit in the voltammetric evolution of the bimetallic surface and its reactivity, evident in Figure S3, was captured by following the peak current density at 0.5 V_{RHE} as the potential limit was raised from 0.75 V_{RHE} to 1.30 V_{RHE}. As shown in Figure 8, the change in behavior is most clearly defined for the Pt films grown using one deposition pulse and decreases in significance for the thicker Pt films. The discontinuity in peak formic acid oxidation current is congruent with recent ICP−MS studies of the dependence of Pt dissolution on the upper potential limit used during voltammetric experiments.[61,62] Specifically, cycling at 10 mV/s in 1.0 or 0.1 mol/L H_2SO_4 to 0.75 V_{RHE} yields negligible Pt dissolution, whereas cycling to 1.3 V_{RHE} results in a mass loss between 3 and 5 ng/cm^2/cycle.[62] Because an idealized close-packed Pt monolayer film corresponds to 486 ng/cm^2, significant impact of Pt dissolution on the formic acid oxidation process is expected within 10−100 voltammetric cycles for the thinnest Pt films examined herein.

The significant improvement in electrocatalysis with cycling called for a more detailed study; thus, the activity of Pt films grown using one deposition pulse were followed during extended voltammetric aging in formic acid. The positive going scans shown in Figure 9a demonstrate the remarkable increase in activity that reaches a peak value after 70 cycles,

DOI: 10.1021/cs501228j
ACS Catal. 2015, 5, 2124−2136

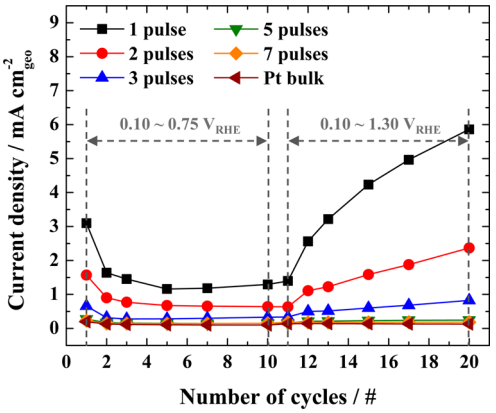

Figure 8. Current density for formic acid oxidation at 0.5 V_{RHE} as a function of the number of deposition pulses used to grow the respective as-deposited films. The upper limit of the voltammetric potential window was increased for all specimens after the 10th cycle.

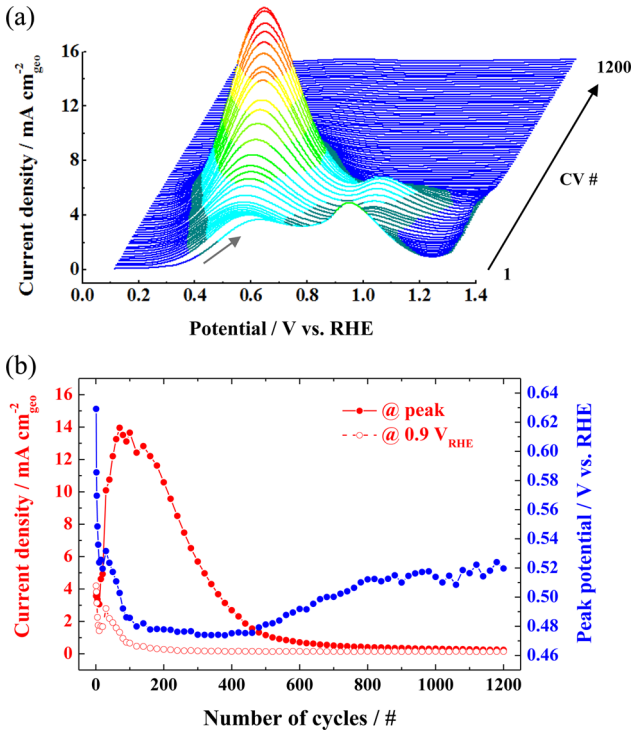

Figure 9. (a) Evolution of formic acid oxidation on Pt during voltammetric cycling at a scan rate of 20 mV/s (only forward scan shown). The as-deposited film was grown using one electrodeposition pulse. (b) The peak potential, current density recorded at the peak potential, and current density at 0.9 V_{RHE} are summarized as a function of the number of cycles.

followed by slow quenching with continued cycling. The trends are well characterized by tracking the peak current and peak potential as a function of the number of cycles, as shown in Figure 9b. Four regimes of behavior are evident. During the first ~100 cycles, the substantial increase in peak current was accompanied by a decrease in the peak potential from 0.63 V_{RHE} to 0.48 V_{RHE}. A monotonic decrease in the second current peak at 0.9 V_{RHE} to background occurred in the same interval, reflecting the attenuation and quenching of the indirect formic acid oxidation path. With continued cycling, the elevated catalytic activity near 0.48 V_{RHE} was sustained, but only for an additional 100 cycles, after which the electrode began to significantly deactivate. Between the 200th and 400th cycle, the peak current decreased to values below that of the original electrode. The decline in activity continued with further cycling, accompanied by a positive shift in the peak potential from 0.47 V_{RHE} to 0.52 V_{RHE} by 1200 cycles.

XPS was used to examine aged electrodes that were representative of various regions of behavior. The individual electrodes were emersed after 70, 200, 400, 800, and 1200 voltammetric cycles, carefully rinsed in H_2-saturated water, and transferred to the XPS spectrometer under an Ar atmosphere. Only half of each as-deposited Pt film were immersed into the formic acid solution for voltammetric cycling, enabling the remaining segment to be used as an internal XPS reference for calibrating the net Pt loss (Figure 10a). Voltammetric aging resulted in a large decrease in the Pt 4f peak intensity and a peak shift to lower binding energy, as evident in Figure 10b. The largest decline in intensity occurred during the first 70 cycles, followed by additional loss through 200 cycles, after which negligible further dissolution was evident. The Pt loss was quantified by comparing the Pt 4f intensity of the exposed region with the adjacent as-deposited material. Assuming the Pt was limited to the surface, the intensity ratio was translated into surface coverage, where the as-deposited material corresponds to a 0.75 surface fraction, as indicated in Figure 10c. Similar results were obtained using the 4f peak intensity ratio for the Pt overlayer and Au substrate in combination with two standard, continuous and fractional, overlayer models.[38,63]

The correspondence between the peak formic acid oxidation current in Figure 9 and the estimated fractional Pt coverage of the aged specimens is summarized in Figure 10d. The maximum peak formic acid oxidation current, observed after 70 voltammetric cycles, corresponds to fractional Pt coverage of 0.28. Normalization of the peak currents to the respective Pt coverage, shown in Figure 10d, indicates the specific activity for formic acid oxidation reaches a maximum value of 50.1 mA/cm^2_{geo}/θ_{Pt} for Pt coverage between 0.28 and 0.21, followed by sharp drop-off in reactivity. This compares well with the optimal coverage of 0.2 recently reported for catalytically active Pt films grown on Au by voltammetric cycling.[19] The surface coverage amounts to Pt loadings of 136 and 102 ng_{Pt}/cm^2, which gives rise to mass specific peak currents between 102 and 103 A/mg_{Pt} for the most catalytically active Pt–Au surfaces. This is a factor of 3.2–9.4 greater than that report for Pt-capped Au nanoparticles.[24]

The peak position of the Pt 4f spectra shown in Figure 10b revealed a distinct shift to lower binding energy as the Pt coverage decreases. The Pt $4f_{7/2}$ shifted from 70.9 eV, a value close to that of bulk Pt for the as-deposited film, to 70.7 eV after 70 cycles to 70.5 eV after 200 cycles with no further changes thereafter. Similar binding energy shifts have been reported for alloys of Pt and Au. For homogeneous alloys, both the Pt 4f and Au 4f binding energy shift position, whereas in the case of Pt surface alloys on Au, the shifts will be weighted significantly, depending on the spatial distribution or subsurface contributions of Pt.[64,65] On the basis of data for metastable Pt–Au alloys produced by cross-beam pulsed laser deposition, the Pt 4f binding energy values for the present films (as-deposited; 70, 200 cycles) would correspond to Pt–Au alloys containing 95%, 66%, and 38% Pt, respectfully.[64] On the other hand, Au surface segregation and alloying both during and following room temperature growth of Pt monolayer films on Au have

DOI: 10.1021/cs501228j
ACS Catal. 2015, 5, 2124–2136

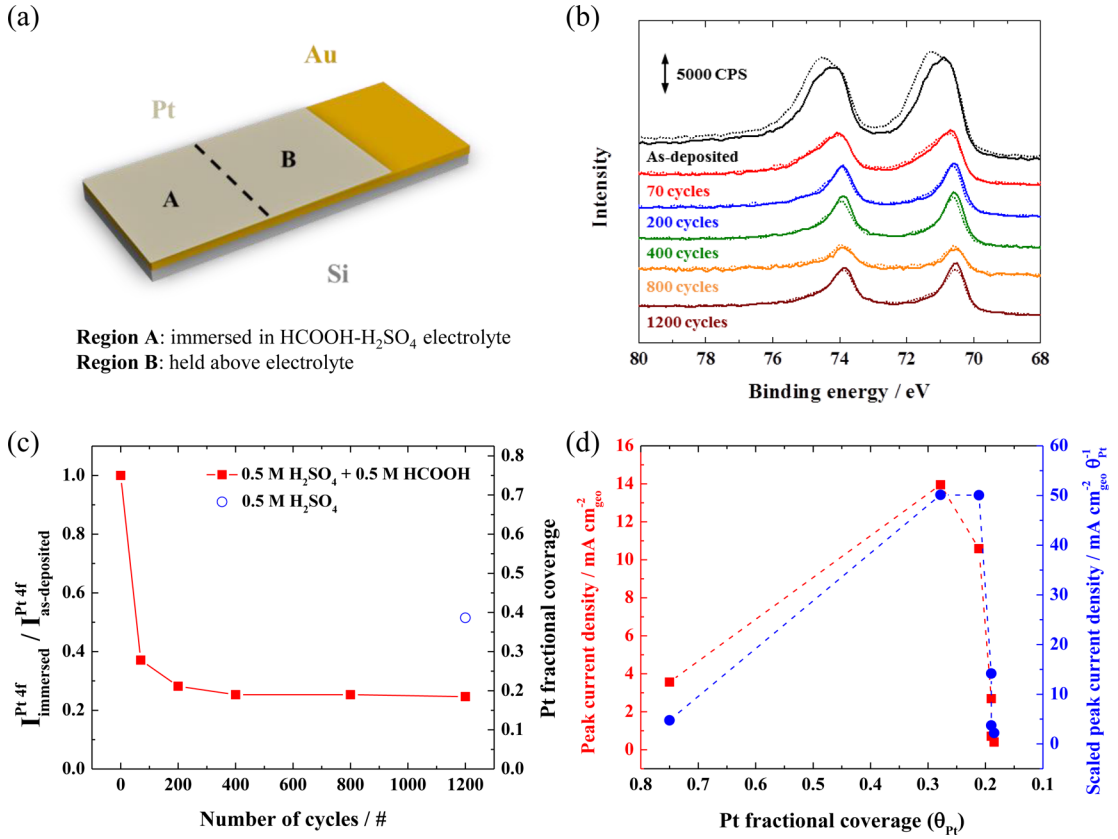

Figure 10. (a) Schematic drawing of the specimen geometry used in XPS in which region A of the Pt overlayer was immersed in HCOOH-H_2SO_4 and region B was held above the electrolyte and used as a reference for the as-deposited state. (b) Pt 4f XPS spectra for films grown using one deposition pulse in the as-deposited state and after 70, 200, 400, 800, and 1200 voltammetric cycles of formic acid oxidation. The solid line spectra were collected immediately after formic acid oxidation; the dotted line spectra were subsequently collected after the specimens were exposed to the laboratory ambient for 24−48 h. (c) The Pt 4f intensity ratio between region A (formic acid oxidation) and region B (as-deposited state) for each specimen as a function of the number of cyclic voltammetric cycles in HCOOH-H_2SO_4. The ordinate on the right side is normalized such that the as-deposited film corresponds to a 0.75 fractional surface coverage. (d) Peak current density (taken from Figure 9) and Pt-coverage-scaled peak current density for formic acid oxidation as a function of the Pt surface coverage.

been reported for both UHV-deposited and electrochemically deposited films and are well supported by theory.[44,55−59,65−67]

Accordingly, the 70.5 eV binding energy has been associated with Pt alloyed into miscut Au (111) surfaces for a nominal Pt fractional coverage that spans the range from 0.4−0.29, depending on the miscut, etc.[65] The depth-convolved nature of XPS hinders a more precise determination of the state and spatial distribution of the Pt in the present system. Nevertheless, as a further probe of the voltammetrically aged Pt films, the specimens were exposed to the laboratory ambient, that is, O_2 and H_2O, and then reexamined by XPS. The corresponding spectra are presented as dotted lines in Figure 10b. Significant oxidation of the as-deposited film was clearly evident, and a more subtle shift was apparent for the 70-cycle film. For films aged to 200 cycles and beyond, the Pt 4f spectra were unaltered by exposure to the atmosphere. The absence of a binding energy shift for these films indicates that surface alloying of Pt with Au makes the films less reactive, or alternatively, Pt may reside in subsurface positions of the alloy that would be protected from O_2. The later configuration is predicted to be the most stable configuration in UHV, although CO, hydrogen, or oxygen species can result in inversion of the relevant segregation energy whence the surface can respond dynamically to changes in the reaction environment.[43,44,55−59,65]

Interestingly, few changes occurred to the chemical state of Pt 4f beyond the 200th cycle, yet the electrocataytic activity for formic acid oxidation was clearly quenched, as shown in Figure 9. XPS revealed the onset and development of a C−O like species on the electrode surface for films aged beyond 200 cycles, as shown in Figure 11a. The C 1s peak with a binding energy near 286 eV, first evident in the spectra for the 400 cycle film, continued to grow with voltammetric aging to 1200 cycles. Because the binding energy and magnitude the Pt 4f did not change between 200th and 400th cycle (Figure 10b), it is reasonable to surmise that the development of the C 1s 286 eV feature is either responsible for or a product of the deactivation of the catalytic activity. The accumulation of the carbon species correlates with the further decrease in the rate of formic acid oxidation, the slow rise of the peak potential shown in Figure 9b.

Examination of the much weaker O 1s spectra, shown in Figure 11b, suggests development of a higher binding energy component, 533−534 eV, that was not evident on the as-deposited material. The ratio of the sensitivity-factor corrected intensity for C 1s and O 1s enables a quick estimate of the stoichiometry of the species in question. Surprisingly, even if one assumes the high binding energy carbon species at 286 eV is bonded to all of the species that comprise the O 1s envelope, an unexpectedly high C/O ratio, >3, was observed that cannot

DOI: 10.1021/cs501228j
ACS Catal. 2015, 5, 2124−2136

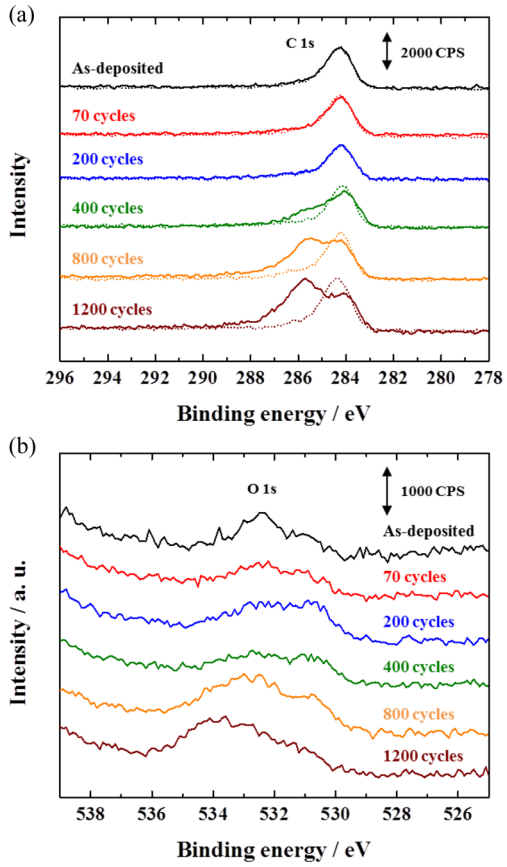

Figure 11. (a) C 1s and (b) O 1s XPS spectra for the one deposition pulse Pt film before and after formic acid oxidation: solid lines from region A (aged in formic acid) and dotted lines from regions B (as-deposited state), see Figure 10a.

be assigned to any known reaction products in the HCOOH-H_2SO_4 system. Rather, the accumulation of some impurity, or its oxidation product (or both), on the surface seems likely. Acetic acid and methyl formate are two common impurities typically associated with formic acid production.[67] For the formic acid used in this study, the upper bound on the acetic acid concentration provided by the manufacturer corresponds to 25 μmol/L in the present experiments. No other organic contaminants were specified. For completeness, no S species were observed in the XPS survey spectra because the sulfate was most likely washed away during the rinsing step.

Varying the voltammetric aging conditions, such as the scan rate, upper potential limit, etc., led to changes in the peak current and the number of cycles required to achieve it (see Figure S4). As in Figure 9a, development of the peak current at 0.5 V_{RHE} was coincident with the disappearance of the CO-related oxidation wave at 0.9 V_{RHE} for all the experimental conditions examined. The number of cycles required to reach the maximum catalytic activity increased with scan rate in a manner congruent with the reported scan rate dependence of Pt dissolution (2.8 μC/cm^2/cycle at 50 mV/s versus 4.6 μC/cm^2/cycle for 10 mV/s in 0.1 mol/L $HClO_4$),[62] suggesting the maximum activity corresponds to similar Pt coverages. However, as shown in Figure S4e, rescaling the abscissa in terms of the total experimental time indicates the decay process follows a $t^{-1/2}$ trend consistent with a diffusion limited process. Because the Pt 4f XPS signal was unaltered while the rate of the formic acid oxidation decreased, it is likely that the deactivation process is due to the accumulation of poisoning impurities manifest by the 286 eV C 1s peak. Assuming the poisoning species blocks the active Pt sites, 5 × 10^{-10} mol/cm^2, at the diffusion-limited rate, a diffusion coefficient of 5 x10^{-6} cm^2/s would correspond to an impurity concentration of 6 μmol/L.[68] The impurities arise from the formic acid or perhaps some trace product of formic acid reduction at the counter electrode.

To further assay the aged electrode surfaces, a parallel experiment was performed in 0.5 mol/L H_2SO_4 to probe the coverage of electroactive Pt species via the H_{upd} and oxide reduction charge and XPS. This enabled the evolution of the Pt overlayer to be partitioned between dissolution and surface alloying. The steady decrease in the H_{upd} and oxide formation and reduction, $Pt_{oxide\ reduction}$ waves with cycling, was readily apparent in Figure 12a,b. The decrease in H_{upd} charge was followed by integrating the total anodic and cathodic current between 0.05 V_{RHE} and 0.40 V_{RHE} and taking the average as shown in Figure 12c. The baseline for a freshly prepared 111 textured Au substrate is also given where the potential induced reconstruction and sulfate adsorption and its order/disorder transition are evident.[69] The H_{upd} charge and $Pt_{oxide\ reduction}$ wave decreased rapidly during the first 200 cycles, followed by a much slower rate beyond 400 cycles. The Pt loss is accompanied by transitions in the shape of the H_{upd} and Pt_{oxide} reduction waves.

The systematic 72% loss of H_{upd} charge that occurs between 0 and 200 cycles corresponds to the conditions associated with the increase in the peak formic acid oxidation current in Figure 9. The subsequent loss of features in the H_{upd} waves after 200 cycles suggests the breakup of any remaining 3-D Pt-rich islands. ICP−MS studies of the dissolution of bulk Pt in 0.1 to 1.0 mol/L H_2SO_4 indicate a rate of mass loss of 3−5 ng/cm^2/cycle.[62] Because the as-deposited Pt film corresponds to 365 ng/cm^2, complete dissolution of the film might be expected to occur within ~121−73 cycles; however, proximity of the Au substrate and alloying provides stabilization against complete dissolution of the Pt. Nevertheless, the ICP−MS metal dissolution studies serve as an excellent basis for predicting the onset of this interesting aging behavior in the heterogeneous Pt overlayer/Au substrate and related systems.

With extended cycling, the voltammetry saturates to yield a capacitive response that is similar but not identical to that of Au as shown in Figure 12b. The broad envelope associated with sulfate adsorption in Au might be present, although the well-defined phase transitions associated with the original Au (111) textured thin film substrate are absent, presumably as a result of Pt alloying and fragmentation of the terraces. Nevertheless, residual activity toward the hydrogen production reflects the influence of the alloyed Pt. The voltammetry is similar to that previously reported for a Pt-decorated Au electrode.[70] After 1200 cycles in 0.5 mol/L H_2SO_4, XPS reveals a 50% loss of Pt 4f intensity and a shift of the peak binding energy to lower values, 70.5 eV, as shown in Figure 12d. The binding energy shift is identical to that observed for the films cycled to and beyond 200 cycles in formic acid solution, indicating a similar final chemical state.

Exposure of the specimen to laboratory ambient resulted in oxidation of the as-deposited segment, but no change was evident for the voltammetrically cycled portion. The lack of oxidation is also congruent with the absence of a voltammetric signature for Pt oxide formation and reduction after 400 voltammetric cycles. In contrast to cycling in HCOOH-H_2SO_4, no significant change in the C 1s spectra was observed

DOI: 10.1021/cs501228j
ACS Catal. 2015, 5, 2124−2136

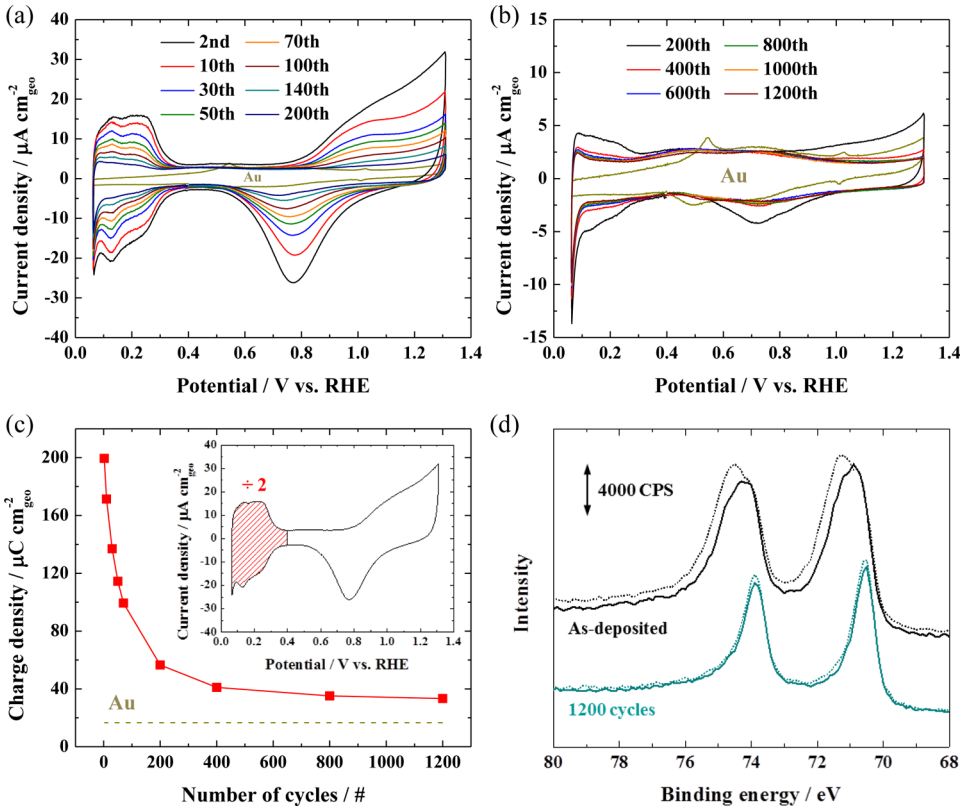

Figure 12. Selected cyclic voltammograms in 0.5 mol/L H_2SO_4 at 20 mV/s for a Pt films deposited using one deposition pulse for (a) 2−200 and (b) 200−1200 cycles. (c) Average charge density of H_{upd} including double layer contributions between 0.05 and 0.40 V_{RHE} as a function of the number of voltammetric cycles. (d) Pt 4f XPS spectra for the one deposition pulse Pt film before and after 1200 cycles in 0.5 mol/L H_2SO_4: solid line spectra are for the results immediately after electrodeposition or following 1200 voltammetric cycle in formic acid (see Figure 10a); dotted line spectra are for the same specimens after subsequent aging in air for 48 h.

following aging in 0.5 mol/L H_2SO_4. As noted earlier, the inertness of the Pt 4f binding energy to air exposure is consistent with stabilization provided by alloying with Au that may also include some Pt being in subsurface positions. Comparing the films aged for 1200 cycles in the presence and absence of formic acid reveals greater dissolution of Pt occurred in the presence of formic acid, with the coverage being half that observed after cycling in H_2SO_4 alone, as shown in Figure 10c. The result is consistent with recent studies of the aging of thicker Pt films indicating that formic acid may play a role in accelerating the Pt dissolution process.[71] Despite the difference in final coverage, similar chemical states of Pt exist on the respective surfaces.

The peak catalytic activity for formic acid oxidation results from the development of Pt−Au ensembles by Pt dissolution and intermixing between the as-deposited Pt overlayer and the Au substrate. The resulting structure favors the direct mechanism of formic acid oxidation, whereas the indirect CO-mediated path is almost completely quenched, as revealed in Figure 9. Operation of the ensemble combines the inability of Au to generate and stabilize CO during formic acid oxidation, with the ability of dilute Pt to catalysis the direct path.[72] The relevance of Pt nearest neighbor effects (e.g., three contiguous Pt atoms required for CO adsorption) has also been previously noted.[73,74] The ensemble effect is also evident for low Pt coverage electrodes with the opposite configuration: namely, Au supported on Pt versus Pt supported on Au.[54] The electronic interactions were very different for these two configurations, yet the formic acid oxidation performance was similar, which indicates the overriding importance of the dilute Pt surface coverage and, by inference, ensemble versus electronic effects. The recent progress in understanding the mechanism of formic acid oxidation in terms of pH effects and the adsorption, conformation and reactivity of the various species on both Pt and Au is sure to stimulate further interest in the Pt−Au bimetallic system.[75−77] Nonetheless, practical implementation of such monolayer bimetallic catalyst will require further study of the relevant durability issues.

4. CONCLUSIONS

A wet form of atomic layer deposition has been used to explore the catalytic activity of ultrathin Pt overlayers on Au for organic fuel oxidation. The use of pulsed electrodeposition enables control of the Pt thickness, thereby facilitating examination of its impact on catalysis. The as-deposited Pt films with a slightly submonolayer coverage exhibited enhanced activity toward methanol oxidation, which is congruent with a recent report of improved activity for Pt films grown on Au (111). The catalytic properties of the as-deposited materials degrade with increasing Pt thickness, and by three monolayers, the catalytic behavior merges with that of bulk Pt. The thickness dependence suggests that exposed Au is important to the superior performance exhibited by the thinnest films (<3 monolayers), although the enhanced activity of the as-deposited thin Pt films was rapidly lost with voltammetric cycling. These observations suggest that the as-deposited mesoscopic structure associated with the step-edge boundary between the high denisty of Pt islands and Au

DOI: 10.1021/cs501228j
ACS Catal. 2015, 5, 2124−2136

substrate was responsible for the enhanced activity toward methanol oxidation.

The activity of the ultrathin Pt films toward the less complex formic acid oxidation reaction was also examined. The as-deposited, submonolayer Pt films produced by one electrodeposition pulse on Au were 20-fold more active than bulk Pt. Bulk Pt behavior was observed for fully coalesced overlayers, with an average thickness near or beyond three monolayers that corresponds to films grown by more than three electrodeposition pulses. The thickness dependence highlights the importance of exposed Au to the enhanced catalytic activity. Voltammetric cycling of the ultrathin Pt films (<3 monolayers) to potentials above 1.15 V_{RHE} leads to significant improvement in the formic acid oxidation performance that is ascribed to a loss of Pt from the surface due to its dissolution and surface alloying between Pt and Au. Enhanced activity in excess of 100-fold over bulk Pt was evidenced for these submonolayer Pt films. The most catalytic electrodes correspond to a Pt fractional surface coverage near 0.2. Coincident with the maximum catalytic activity was the absence of the second oxidation peak at 0.9 V_{RHE} that relates to CO poisoning of bulk Pt electrodes. In contrast to methanol oxidation, fragmentation of the as-deposited Pt monolayer films leads to enhanced performance for formic acid oxidation that is facilitated by an ensemble effect associated with the mixed Pt−Au surface. Unfortunately, the activated low coverage Pt−Au alloy phase is subject to deactivation by carbon-based adsorbates that accumulate from impurities either in the formic acid or generated by reactions within the electrochemical cell. Further work will be required to secure the performance gains that can be realized with the bimetallic Pt−Au ensembles.

■ ASSOCIATED CONTENT

Supporting Information

The following file is available free of charge on the ACS Publications website at DOI: 10.1021/cs501228j.

Cyclic voltammetry for H_{upd}, methanol oxidation, and formic acid oxidation on Pt ultrathin films and bulk Pt (PDF)

■ AUTHOR INFORMATION

Corresponding Author

*E-mail: thomas.moffat@nist.gov.

Notes

The authors declare no competing financial interest.

■ ACKNOWLEDGMENTS

This work was supported by the NIST Material Measurement Laboratory programs. The X-ray photoelectron spectrometer was provided by NIST American Recovery and Reinvestment Act funds. Identification of commercial products in this paper is done to specify the experimental procedure. In no case does this imply endorsement or recommendation by the National Institute of Standards and Technology.

■ REFERENCES

(1) *Fuel Cell Catalysis: A Surface Science Approach*; Koper, M. T. M., Ed.; Wiley: Hoboken, N.J., 2009; and references therein.

(2) Jarvi, T. D.; Stuve, E. M. *Electrocatalysis*; Lipkowski, J., Ross, P. N., Eds.; Wiley-VCH: New York, 1998; pg 75−154; and references therein.

(3) Zhao, X.; Yin, M.; Ma, L.; Liang, L.; Liu, C.; Liao, J.; Lu, T.; Xing, W. *Energy Environ. Sci.* **2011**, *4*, 2736−2753.

(4) Yu, X.; Pickup, P. G. *J. Power Sources* **2008**, *182*, 124−132.

(5) Clavilier, J.; Lamy, C.; Leger, J. M. *J. Electroanal. Chem.* **1981**, *125*, 249−254.

(6) Clavilier, J.; Parsons, R.; Durand, R.; Lamy, C.; Leger, J. M. *J. Electroanal. Chem.* **1981**, *124*, 321−326.

(7) Adzic, R. R.; Tripković, A. V.; O'Grady, W. E. *Nature* **1982**, *296*, 137−138.

(8) Xia, X. H.; Iwasita, T.; Ge, F.; Vielstich, W. *Electrochim. Acta* **1996**, *41*, 711−718.

(9) Grozovski, V.; Solla-Gullon, J.; Climent, V.; Herrero, E.; Feliu, J. M. *J. Phys. Chem. C* **2010**, *114*, 13802−13812.

(10) Li, M.; Liu, P.; Adzic, R. R. *J. Phys. Chem. Lett.* **2012**, *3*, 3480−3485.

(11) Kumar, S.; Zou, S. *Langmuir* **2007**, *23*, 7365−7371.

(12) Du, B.; Tong, Y. *J. Phys. Chem. B* **2005**, *109*, 17775−17780.

(13) Ataee-Esfahani, H.; Wang, L.; Nemoto, Y.; Yamauchi, Y. *Chem. Mater.* **2010**, *22*, 6310−6318.

(14) Kim, J.; Jung, C.; Rhee, C. K.; Lim, T. *Langmuir* **2007**, *23*, 10831−10836.

(15) Khosravi, M.; Amini, M. K. *Int. J. Hydrogen Energy* **2010**, *35*, 10527−10538.

(16) Jia, J.; Cao, L.; Wang, Z. *Langmuir* **2008**, *24*, 5932−5936.

(17) Zeng, J.; Yang, J.; Lee, J. Y.; Zhou, W. *J. Phys. Chem. B* **2006**, *110*, 24606−24611.

(18) Fang, P.; Duan, S.; Lin, X.; Anema, J. R.; Li, J.; Buriez, O.; Ding, Y.; Fan, F.; Wu, D.; Ren, B.; Wang, Z. L.; Amatore, C.; Tian, Z. *Chem. Sci.* **2011**, *2*, 531−539.

(19) Obradović, M. D.; Tripković, A. V.; Gojković, S. L. *Electrochim. Acta* **2009**, *55*, 204−209.

(20) Wang, R.; Wang, C.; Cai, W.; Ding, Y. *Adv. Mater.* **2010**, *22*, 1845−1848.

(21) Kristian, N.; Yu, Y.; Gunawan, P.; Xu, R.; Deng, W.; Liu, X.; Wang, X. *Electrochim. Acta* **2009**, *54*, 4916−4924.

(22) Kristian, N.; Yan, Y.; Wang, X. *Chem. Commun.* **2008**, 353−355.

(23) Yu, Y.; Hu, Y.; Liu, X.; Deng, W.; Wang, X. *Electrochim. Acta* **2009**, *54*, 3092−3097.

(24) Zhang, G−R.; Zhao, D.; Feng, Y−Y.; Zhang, B.; Su, D. S.; Liu, G.; Xu, B−Q. *ACS Nano* **2012**, *6*, 2226−2236.

(25) Wang, R.; Liu, J.; Liu, P.; Bi, X.; Yan, X.; Wang, W.; Ge, X.; Chen, M.; Ding, Y. *Chem. Sci.* **2014**, *5*, 403−409.

(26) Podlovchenko, B. I.; Maksimov, Y. M.; Maslakov, K. I. *Electrochim. Acta* **2014**, *130*, 351−360.

(27) Scheijen, F. J. E.; Beltramo, G. L.; Hoeppener, S.; Housmans, T. H. M.; Koper, M. T. M. *J. Solid State Electrochem.* **2008**, *12*, 483−495.

(28) Mavrakakis, M.; Hammer, B.; Nørskov, J. K. *Phys. Rev. Lett.* **1998**, *81*, 2819−2822.

(29) Speder, J.; Altmann, L.; Bäumer, M.; Kirkensgaard, J. J. K.; Mortensen, K.; Arenz, M. *RSC Adv.* **2014**, *4*, 14971−14978.

(30) Debe, M. K. *Nature* **2012**, *486*, 43−51.

(31) Fayette, M.; Liu, Y.; Bertrand, D.; Nutariya, J.; Vasiljevic, N.; Dimitrov, N. *Langmuir* **2011**, *27*, 5650−5658.

(32) Brankovic, S. R.; Wang, J. X.; Adzic, R. R. *Surf. Sci.* **2001**, *474*, L173−L179.

(33) Mrozek, M. F.; Xie, Y.; Weaver, M. J. *Anal. Chem.* **2001**, *73*, 5953−5960.

(34) Kim, Y.-G.; Kim, J. Y.; Vairavapandian, D.; Stickney, J. L. *J. Phys. Chem. B* **2006**, *110*, 17998−18006.

(35) Liu, Y.; Gokcen, D.; Bertocci, U.; Moffat, T. P. *Science* **2012**, *338*, 1327−1330.

(36) Liu, Y.; Hangarter, C. M.; Garcia, D.; Moffat, T. P. *Surf. Sci.* **2014**, *631*, 141−154.

(37) ASTM E 2108-00 Standard Practice for Calibration of the Electron Binding Energy Scale of an X-ray Photoelectron Spectrometer.

(38) Cumpson, P. J.; Seah, M. P. *Surf. Interface Anal.* **1997**, *25*, 430−446.

DOI: 10.1021/cs501228j
ACS Catal. 2015, 5, 2124−2136

(39) Strmcnik, D.; Tripkovic, D.; van der Vliet, D.; Stamenkovic, V.; Markovic, N. M. *Electrochem. Commun.* **2008**, *10*, 1602−1605.
(40) Karlberg, G. S.; Jaramillo, T. F.; Shúlason, E.; Rossmeisl, J.; Bligaard, T.; Nørskov, J. K. *Phys. Rev. Lett.* **2007**, *99*, 126101−126101(4).
(41) Tan, T. L.; Wang, L.; Johnson, D. D.; Bai, K. *J. Phys. Chem. C* **2013**, *117*, 22696−22704.
(42) Climent, V.; Feliu, J. M. *J. Solid State Electrochem.* **2011**, *15*, 1297−1315 and references therein .
(43) Abrams, B. L.; Vesborg, P. C. K.; Bonde, J. L.; Jaramillo, T. F.; Chorkendorff, I. *J. Electrochem. Soc.* **2009**, *156*, B273−B282.
(44) Pedersen, M. Ø.; Helveg, S.; Ruban, A.; Stensgaard, I.; Lægsgaard, E.; Nørskov, J. K.; Besenbacher, F. *Surf. Sci.* **1999**, *426*, 395−409.
(45) Fayette, M.; Liu, Y.; Bertrand, D.; Nutariya, J.; Vasiljevic, N.; Dimitrov, N. *Langmuir* **2011**, *27*, 5650−5658.
(46) Brankovic, S. R.; Wang, J. X.; Adzic, R. R. *Surf. Sci.* **2001**, *474*, L173−L179.
(47) Hwang, S.; Bonevich, J. E.; Kim, J. J.; Moffat, T. P. *J. Electrochem. Soc.* **2011**, *158*, D307−D316.
(48) Rossmeisl, J.; Ferrin, P.; Tritsaris, G. A.; Nilekar, A. U.; Koh, S.; Bae, S. E.; Brankovic, S. R.; Strasser, P.; Mavrikakis, M. *Energy Environ. Sci.* **2012**, *5*, 8335−8342.
(49) Grozovski, V.; Climent, V.; Herrero, E.; Feliu, J. M. *J. Electroanal. Chem.* **2011**, *662*, 43−51.
(50) Lee, S. W.; Chen, S.; Sheng, W.; Yabuuchi, N.; Kim, Y.; Mitani, T.; Vescovo, E.; Shao-Horn, Y. *J. Am. Chem. Soc.* **2009**, *131*, 15669−15677.
(51) Bae, S.; Gokcen, D.; Liu, P.; Mohammadi, P.; Brankovic, S. R. *Electrocatal.* **2012**, *3*, 203−210.
(52) Santana, J. A.; Kruger, S.; Rosch, N. *J. Phys. Chem. C* **2014**, *118*, 22102−22110.
(53) Stolbov, S.; Zuluaga, S. *J. Phys. Chem. Lett.* **2013**, *4*, 1537−1540.
(54) Suntivich, J.; Xu, Z.; Carlton, C. E.; Kim, J.; Han, B.; Lee, S. W.; Bonnet, N.; Marzari, N.; Allard, L. F.; Gasteiger, H. A.; Hamad−Schifferli, K.; Shao−Horn, Y. *J. Am. Chem. Soc.* **2013**, *135*, 7985−7991.
(55) Gohda, Y.; Groβ, A. *J. Electroanal. Chem.* **2007**, *607*, 47−53.
(56) Gohda, Y.; Groβ, A. *Surf. Sci.* **2007**, *601*, 3702−3706.
(57) Leppert, L.; Albuquerque, R. Q.; Foster, A. S.; Kümmel, S. *J. Phys. Chem. C* **2013**, *117*, 17268−17273.
(58) Prieto, M. J.; Tremilio-Filho, G. *Phys. Chem. Chem. Phys.* **2013**, *15*, 13184−13189.
(59) Tereshchuk, P.; Freire, R. L. H.; Da Silva, J. L. F. *RSC Adv.* **2014**, *4*, 9247−9254.
(60) Solla−Gullón, J.; Aldaz, A.; Clavilier, J. *Electrochim. Acta* **2013**, *87*, 669−675.
(61) Topalov, A. A.; Katsounaros, I.; Auinger, M.; Cherevko, S.; Meier, J. C.; Klemm, S. O.; Mayrhofer, K. J. J. *Angew. Chem., Int. Ed.* **2012**, *51*, 12613−12615.
(62) Topalov, A. A.; Cherevko, S.; Zeradjanin, A. R.; Meier, J. C.; Katsounaros, I.; Mayrhofer, K. J. J. *Chem. Sci.* **2014**, *5*, 631−638.
(63) *Surface Analysis by Auger and X-ray Photoelectron Spectroscopy*; Briggs, D., Seah, M. P., Eds.; John Wiley& Sons: New York, NY, 1987.
(64) Irissou, E.; Laplante, F.; Garbarino, S.; Chaker, M.; Guay, D. *J. Phys. Chem. C* **2010**, *114*, 2192−2199.
(65) Prieto, M. J.; Carbonio, E. A.; Fatayer, S.; Landers, R.; de Siervo, A. *Phys. Chem. Chem. Phys.* **2014**, *16*, 13329−13339.
(66) Schmickler, W.; Pötting, K.; Mariscal, M. *Chem. Phys.* **2006**, *320*, 149−154.
(67) Law, W. L.; Platt, A. M.; Wimalaratne, P. D. C.; Blair, S. L. *J. Electrochem. Soc.* **2009**, *156*, B553−B557.
(68) Rouhana, L. L.; Moussallem, M. D.; Schlenoff, J. B. *J. Am. Chem. Soc.* **2011**, *133*, 16080−16091.
(69) Zhumaev, U.; Rudnev, A. V.; Li, J.; Kuzume, A.; Vu, T.; Wandlowski, T. *Electrochim. Acta* **2013**, *112*, 853−863.
(70) Strbac, S.; Petrovic, S.; Vasilic, R.; Kovac, J.; Zalar, A.; Rakocevic, Z. *Electrochim. Acta* **2007**, *53*, 998−1005.
(71) Fayette, M.; Nutariya, J.; Vasiljevic, N.; Dimitrov, N. *ACS Catal.* **2013**, *3*, 1709−1718.
(72) Cuesta, A.; Cabello, G.; Hartl, F. W.; Escudero-Escribano, M.; Vaz-Dominguez, C.; Kibler, L. A.; Osawa, M.; Gutiérrez, C. *Catal. Today* **2013**, *202*, 79−86.
(73) Cuesta, A. *J. Am. Chem. Soc.* **2006**, *128*, 13332−13333.
(74) Cuesta, A.; Escudero, M.; Lanova, B.; Baltruschat, H. *Langmuir* **2009**, *25*, 6500−6507.
(75) Joo, J.; Uchida, T.; Cuesta, A.; Koper, M. T. M.; Osawa, M. *Electrochim. Acta* **2014**, *129*, 127−136.
(76) Brimaud, S.; Solla−Gullon, J.; Weber, I.; Feliu, J. M.; Behm, R. J. *ChemElectroChem* **2014**, *1*, 1075−1083.
(77) Gao, W.; Song, E. H.; Jiang, Q.; Jacob, T. *Chem.—Eur. J.* **2014**, *20*, 11005−11012.

DOI: 10.1021/cs501228j
ACS Catal. 2015, 5, 2124−2136